MNRAS **483,** 3878–3887 (2019)
Advance Access publication 2018 December 20

doi:10.1093/mnras/sty3395

The clustering of the SDSS-IV extended Baryon Oscillation Spectroscopic Survey DR14 quasar sample: measuring the evolution of the growth rate using redshift-space distortions between redshift 0.8 and 2.2

Rossana Ruggeri,[1★] Will J. Percival,[1] Héctor Gil-Marín,[2,3] Florian Beutler,[1,4] Eva-Maria Mueller,[1] Fangzhou Zhu,[5] Nikhil Padmanabhan,[5] Gong-Bo Zhao,[1,6] Pauline Zarrouk,[7] Ariel G. Sánchez,[8] Julian Bautista,[9] Jonathan Brinkmann,[10] Joel R. Brownstein,[9] Falk Baumgarten,[11] Chia-Hsun Chuang,[11,12] Kyle Dawson,[9] Hee-Jong Seo,[13] Rita Tojeiro[14] and Cheng Zhao[15]

[1]*Institute of Cosmology & Gravitation, University of Portsmouth, Dennis Sciama Building, Portsmouth PO1 3FX, UK*
[2]*Sorbonne Universites, Institut Lagrange de Paris (ILP), 98 bis Boulevard Arago, F-75014 Paris, France*
[3]*Laboratoire de Physique Nucleaire et de Hautes Energies, Universit ´e Pierre et Marie Curie, 4 Place Jussieu, F-75005 Paris, France*
[4]*Lawrence Berkeley National Lab, 1 Cyclotron Rd, Berkeley, CA 94720, USA*
[5]*Dept. of Physics, Yale University, New Haven, CT 06511, USA*
[6]*National Astronomy Observatories, Chinese Academy of Science, Beijing 100012, P.R.China*
[7]*IRFU,CEA, Université Paris-Saclay, F-91191 Gif-sur-Yvette, France*
[8]*Max-Planck-Institut für extraterrestische Physik, Postfach 1312, Giessenbachstr, D-85741 Garching, Germany*
[9]*Department of Physics and Astronomy, University of Utah, 115 S. 1400 E., Salt Lake City, UT 84112, USA*
[10]*Apache Point Observatory, P.O. Box 59, Sunspot, NM 88349, USA*
[11]*Leibniz-Institut für Astrophysik Potsdam (AIP), An der Sternwarte 16, D-14482 Potsdam, Germany*
[12]*Kavli Institute for Particle Astrophysics and Cosmology & Physics Department, Stanford University, Stanford, CA 94305, USA*
[13]*Department of Physics and Astronomy, Ohio University, Clippinger Labs, Athens, OH 45701, USA*
[14]*School of Physics and Astronomy, University of St Andrews, North Haugh, St Andrews KY16 9SS, UK*
[15]*Tsinghua Center for Astrophysics and Department of Physics, Tsinghua University, Beijing 100084, China*

Accepted 2018 November 29. Received 2018 November 21; in original form 2018 February 8

ABSTRACT

We measure the growth rate and its evolution using the anisotropic clustering of the extended Baryon Oscillation Spectroscopic Survey (eBOSS) Data Release 14 (DR14) quasar sample, which includes 148 659 quasars covering the wide redshift range of $0.8 < z < 2.2$ and a sky area of 2112.90 deg^2. To optimize measurements we deploy a redshift-dependent weighting scheme, which allows us to avoid binning and perform the data analysis consistently including the redshift evolution across the sample. We perform the analysis in Fourier space, and use the redshift evolving power spectrum multipoles to measure the redshift-space distortion parameter $f\sigma_8$ and parameters controlling the anisotropic projection of the cosmological perturbations. We measure $f\sigma_8(z = 1.52) = 0.43 \pm 0.05$ and $\mathrm{d}f\sigma_8/\mathrm{d}z\,(z = 1.52) = -0.16 \pm 0.08$, consistent with the expectation for a lambda cold dark matter cosmology as constrained by the Planck experiment.

Key words: cosmology: observations – dark energy – dark matter – large-scale structure of Universe.

1 INTRODUCTION

The positions of galaxies signpost peaks in the density field, and consequently measuring their clustering provides a wealth of cosmological information. Two components of the clustering are particularly important: baryon acoustic oscillations (BAO) act as a robust standard ruler, allowing geometrical measurements from measurements of their projected sizes, while redshift-space distortions (RSD) change the clustering amplitude in a way that is anisotropic around the line of sight. The strength of the RSD signal depends on the rate of structure growth at the redshifts of the galaxies, and therefore allows tests of general relativity on extremely large scales. The combination of these measurements is able to distinguish

★ E-mail: rossana.ruggeri@port.ac.uk

between competing models of dark energy, the phenomenon driving the accelerated expansion of the Universe.

Dark energy starts to dominate the Universe at a redshift $z \sim 0.7$ and, in order to understand the physics behind this in detail, we desire BAO and RSD measurements covering a wide range of redshifts. In particular, measurements at redshifts significantly greater than 0.7 allow us to measure the amplitude of fluctuations before dark energy dominates, normalizing measurements of acceleration at lower redshifts. The extended Baryon Oscillation Spectroscopic Survey (eBOSS; Dawson et al. 2016), part of the SDSS-IV experiment (Blanton et al. 2017), was designed with this specific goal in mind (Zhao et al. 2016), with the dominant target for observations being quasars between the redshifts of $0.8 < z < 2.2$, at a relatively low density of 82.6 /deg^2.

We expect significant evolution in such a sample with redshift; for example, the bias of these quasars is expected to evolve as $b(z) \simeq 0.28[(1+z)^2 - 6.6] + 2.4$ (Croom et al. 2004; Laurent et al. 2017), thus ranging from 1.6 to 3.4 across the survey. Consequently, when analysing data we need to be careful to allow for this evolution, both when optimizing any kind of analysis as well as to make sure the measurements are unbiased. The method of 'redshift weights' does this by constructing sets of weights applied to all of the data, before calculating clustering statistics (such as the power spectrum multipoles). The weights are designed to allow the optimal measurement of evolving cosmological parameters. The cosmological parameters could be, for example, the coefficients of a Taylor expansion of the growth rate with redshift.

Zhu, Padmanabhan & White (2015), Ruggeri et al. (2017b), and Mueller, Percival & Ruggeri (2017) calculated and analysed weights optimized to measure the distance–redshift relation from BAO, the growth rate from RSD, and primordial non-Gaussianity from the large-scale bias, respectively. Recently, these ideas were applied to mock catalogues for BAO (Zhu et al. 2016) and RSD (Ruggeri et al. 2017a), demonstrating their potential. The technique is now ready to be applied to data, and the characteristics of the eBOSS quasar sample make it the ideal choice for such analysis. In a companion paper, Zhu et al. (2018), a similar technique is applied to measure the BAO, whereas we instead focus here on RSD measurements. In Zhao et al. (2018) and Wang et al. (2018), a different methodology is used to measure the evolving RSD and BAO signals: standard measurements are made as if for a narrow redshift interval, but instead for weighted distributions of the quasars. A cosmological model can be tested using the supplied sets of weights to determine the effective RSD and BAO in the model given that kernel, and comparing to the corresponding measurements.

In our paper, we apply the method presented in Ruggeri et al. (2017a), and consider two sets of weights designed to test for deviations from the lambda cold dark matter (ΛCDM) model, by altering $\Omega_{\rm m}(z)$ or $f\sigma_8(z)$. The first choice can change both growth and geometry, unless we explicitly fix one of these, while the second only tests the cosmological growth rate. We also consider a traditional analysis, where we only apply weights matching those of Feldman, Kaiser & Peacock (1994). This corresponds to a limit of the redshift-weighting approach as the redshift weights tend towards the FKP form in the limit where the error associated with a cosmological parameter does not vary with redshift. Our paper is laid out as follows: in Section 2 we briefly review the eBOSS data. Section 3 provides an overview of the method, focussing on the eBOSS specific aspects. The results are presented in Section 5, and discussed in Section 6.

2 THE EBOSS DR14 DATA SET

The eBOSS survey (Dawson et al. 2016; Zhao et al. 2016) will provide a redshift survey covering the largest volume to date at a density where it can provide useful cosmological measurements. Full survey details can be found in Dawson et al. (2016); observations will ultimately include 250 000 luminous red galaxies (LRGs), 195 000 emission-line galaxies (ELGs), and over 500 000 quasars. The main goal is to make BAO distance measurements at 1–2 per cent accuracy (Zhao et al. 2016). Using the same samples the goal for the RSD analysis is to constrain $f\sigma_8$ at 2.5 per cent, 3.3 per cent, and 2.8 per cent accuracy for LRGs, ELGs, and quasars, respectively. For the current analysis we use the quasar catalogues from the eBOSS DR14 (Pâris et al. 2017) data set. The target selection algorithm is presented in Myers et al. (2015); quasars were selected from the combination of SDSS imaging data (Aihara et al. 2011) and that from the WISE satellite (Wright et al. 2010). The SDSS imaging data were taken using the Sloan telescope (Gunn 1998; Gunn et al. 2006), and spectra were taken using the BOSS spectrographs (Smee et al. 2013). Redshifts were measured using the standard BOSS pipeline (Bolton et al. 2012), coupled with various updates and visual inspection of a subset as outlined in Pâris et al. (2017), which describes the DR14Q quasar catalogue.

The quasar sample covers a wide redshift range, $0.8 < z < 2.2$, with a low density, 82.6/deg^2, compared with other targets, and is designed to ultimately cover a total area of 7500 deg^2. In this paper we use the intermediate data sample referred to as DR14 (Pâris et al. 2017). This sample contains 98 577 quasars covering the wide redshift range of $0.8 < z < 2.2$ and a sky area of 1001.25 deg^2. Early measurements of the bias of this sample are presented in Laurent et al. (2017), showing excellent agreement with those measured from earlier catalogues (Croom et al. 2004). In this work we use the *fiducial* redshift estimates, obtained as a combination of the three different estimates ($z_{\rm Mg\,II}$, $z_{\rm PCA}$, $z_{\rm PL}$), presented in Pâris et al. (2017) and we show the constraints obtained when measuring the full NGC + SGC samples. The comparison between the results from different redshift estimates and the discussion for the analysis on NGC (SGC) only is presented in Zarrouk et al. (2018) and Gil-Marín et al. (2018).

We apply a number of weights in order to correct for various features of the data. First, we apply a set of systematics weights designed to correct for trends observed in the target catalogue, where the density of targets varies with observational parameters. These weights are presented in Zarrouk et al. (2018) and our treatment is consistent with this. We upweight the nearest neighbour to correct for close-pairs. Redshift failures are corrected by downweighting the random catalogue used to define the survey mask, as a function of the plate position, which alters the expected signal-to-noise ratio (Zarrouk et al. 2018). In addition, we apply redshift-dependent weights optimized to measure the value and derivative of a cosmological parameter [chosen to be $\Omega_{\rm m}(z)$ or $f\sigma_8(z)$] beyond a fiducial ΛCDM model, around a pivot redshift. The design of these weights considers the information available and the dependence on the cosmological parameter of interest. For the eBOSS quasar data, it is not useful to probe beyond the first derivative of the parameters around a pivot redshift because of the limited constraining power of the data set. The derivation of the weights was presented in Ruggeri et al. (2017a).

In the following sections we briefly review the key points of the analysis.

3 MODELLING THE DATA

We contrast three methods:

(i) A traditional analysis, fitting with one set of weights, matching those introduced by Feldman et al. (1994), commonly known as FKP weights.

(ii) Redshift-weighted, with two sets of weights optimized to measure $\Omega_{\rm m}(z)$; we refer to this method also as $w_{\Omega_{\rm m}}$.

(iii) Redshift-weighted, with two sets of weights optimized to measure $f\sigma_8(z)$; we refer to this method also as $w_{f\sigma_8}$.

We perform fits either allowing the anisotropic geometrical projection parameters (also know as the AP parameters (Alcock & Paczynski 1979), $\alpha_{\shortparallel}$ and $\alpha_{\perp}$ to be simultaneously fitted, or keeping them fixed at their fiducial value.

We derive and fit models for all three of these methods using the same procedure, as described in Ruggeri et al. (2017a). Briefly, we calculate the TNS model (Taruya, Nishimichi & Saito 2010) for each model to be tested at a discrete series of redshifts and apply the redshift weights to give models of the redshift-space moments.

In order to account for the coupling between redshift evolution in the cosmological parameters and the survey geometry on the power spectra moments we discretize the window convolution, creating sub-windows at redshifts 0.87, 1.01, 1.15, 1.29, 1.43, 1.57, 1.71, 1.85, 1.99, 2.13, following the procedure described in Ruggeri et al. (2017b).

The TNS model includes corrections from the non-linear coupling between the density and velocity fields, it requires us to calculate the non-linear matter power spectra, $P_{\delta\delta}$, $P_{\delta\theta}$, $P_{\theta\theta}$, which we do at one-loop order in standard perturbation theory (SPT) using the linear power spectrum output from CAMB (Lewis & Bridle 2002). We refer to Ruggeri et al. (2017a) for a larger description of the TNS model.

Quasar bias is modelled including non-local contributions (Baldauf et al. 2012; Chan, Scoccimarro & Sheth 2012), with parameters corresponding to the linear b, second-order local b_2, non local $b_{\rm s2}$, and the third-order non-local $b_{\rm 3nl}$ bias parameters. We make the approximations $b_{\rm s2} = -4(b-1)/7$ and $b_{\rm 3nl} = 32(b-1)/315$ following Baldauf et al. (2012) and Saito et al. (2014), respectively; we fit only a local bias model as the quasar data do not contain enough small-scale information to fit for non-local bias parameters. We assume b linearly evolves with redshift, and that b_2 does not vary with redshift. In fact we know that the bias evolves strongly with redshift (Croom et al. 2004; Laurent et al. 2017) but, given that we wish to constrain cosmological evolution across the sample, this should be simultaneously fitted with the cosmological measurements to avoid double-counting information. We perform a linear fit to match the linear cosmological measurements as a Taylor expansion with respect to the value of $b\sigma_8$ at the pivot redshift,

$$b\sigma_8(z) = b\sigma_8(z_{\rm p}) + \partial b\sigma_8/\partial z|_{z_{\rm p}}(z - z_{\rm p}). \quad (1)$$

With $b\sigma_8(z_{\rm p})$ and $\partial b\sigma_8/\partial z|_{z_{\rm p}}$ free parameters. We also fit for a constant shot noise term S.

The *traditional analysis*, method (i), makes measurements at a single effective epoch ($z_{\rm p} = 1.52$), using only FKP weights, so we have a single-weighted monopole moment, and a single-weighted quadrupole moment to be fitted with five free parameters in total: $f\sigma_8$, $b\sigma_8$, $\sigma_{\rm FoG}$, $b_2\sigma_8$, S, where S accounts for deviations from the Poisson shot noise and $\sigma_{\rm FoG}$ is a phenomenological parameter from the TNS model.

When allowing the background geometry to vary, this parameter set is extended to seven, $f\sigma_8$, $b\sigma_8$, $\sigma_{\rm FoG}$, $b_2\sigma_8$, S, $\alpha_{\shortparallel}$, $\alpha_{\perp}$, including the projection parameters. To validate this model we fitted to a single snapshot drawn from the Outerim simulation (Habib et al. 2016), with results presented in Zarrouk et al. (2018). Good agreement was recovered. We compare our traditional measurement with other results obtained from similar analyses in Zarrouk et al. (2018), Hou et al. (2018), Gil-Marín et al. (2018), and Zhao et al. (2018).

Method (ii) explores deviations from ΛCDM through the evolution of $\Omega_{\rm m}$ in redshift. To do so we model $\Omega_{\rm m}(z)$ as a Taylor expansion about the fiducial model $\Omega_{\rm m,fid}$,

$$\Omega_{\rm m}(z) = \Omega_{\rm m,fid}q_0[1 + q_1 y(z)] \quad (2)$$

with $y(z) = \Omega_{\rm m,fid}(z)/\Omega_{\rm m,fid}(z_{\rm p})$; q_0 and q_1 are free parameters giving the overall normalization and first derivative of $\Omega_{\rm m}(z)$ at the pivot redshift. In this work, we use a pivot redshift $z_{\rm p} = 1.52$, matching the effective redshift of the quasar sample.[1] To test the robustness of the analysis we perform the same analysis selecting $z_{\rm p} = 1.1$ and $z_{\rm p} = 1.7$ confirming that there is no dependence on the pivot redshift selected; for this method we have two sets of weights for the monopole and two sets for the quadrupole, so we simultaneously fit to four moments in total.

This parametrization provides a common framework to test for deviations from the fiducial cosmology both in terms of geometry (distance–redshift relation) and growth rate ($f\sigma_8$), by considering these quantities as a function of $\Omega_{\rm m}(q_0, q_1)$. The strategy is to assume that, for expected small deviations, the standard equations, linking the Hubble parameter and the Angular Diameter distance to $\Omega_{\rm m}(z)$, are the same as in the ΛCDM model.

This is discussed further in Ruggeri et al. (2017b). Once we have measured q_0, and q_1, we can project them back to $\alpha_{\shortparallel}$, $\alpha_{\perp}$, and $f\sigma_8$ at any epoch. The physical limit that $\Omega_{\rm m}$ cannot be negative at any epoch places a physical motivated prior on $\alpha_{\shortparallel}$, $\alpha_{\perp}$, and $f\sigma_8$; the impact of such priors is discussed in detail in Section 5.

The third parametrization, method (iii), explores the evolution of $f\sigma_8$; it represents a more direct way to measure deviations in structure growth, where the latter are artificially kept separate from the geometrical evolution. Here we directly Taylor expand $f\sigma_8(z)$

$$[f\sigma_8](z) = [f\sigma_8]_{\rm fid}(z)p_0[1 + p_1 x(z)], \quad (3)$$

where $x = [f\sigma_8]_{\rm fid}(z)/[f\sigma_8]_{\rm fid}(z_{\rm p})$, and p_0 and p_1 are free parameters giving the overall normalization and first derivative of $f\sigma_8(z)$ at the pivot redshift. This model allows a wider range of deviations from the ΛCDM scenario, as it does not assume any particular form or relation for f and σ_8. For this method we have two sets of weights for the monopole and two sets of the quadrupole, so we simultaneously fit to four moments in total.

In Ruggeri et al. (2017a), we compare the *traditional analysis* to the measurement from the redshift weights techniques projected at the pivot redshift using mock catalogues, confirming that the redshift weights analysis give unbiased constraints. Weights optimized to look for deviations from ΛCDM using changes in either $\Omega_{\rm m}$ or $f\sigma_8$, provide complementary measurements given the different deviations, and dependencies on observations. Both can be used to measure $f\sigma_8$ at any particular redshift, and be compared to the more traditional way of looking for deviations.

[1] The effective redshift is defined as the weighted mean of all the redshifts of the sample.

4 FITTING MODELS TO THE DATA

We now fit to the quasar data with each of the three models, traditional, $\Omega_m, f\sigma_8$, described in Section 3. We fit to the NGC and SGC data independently, assuming they are uncorrelated, a reasonable assumption given their physical separation, and then combine the likelihoods to give our result from the full NGC + SGC sample. The results presented in the following sections have been obtained by simultaneously fitting the full set of parameters using an MCMC approach, and then marginalizing over the parameters not plotted or measured, including the nuisance parameters S and σ_{FoG}, common to all methods. We measure the weighted moments of the power spectrum, using the method described in Bianchi et al. (2015), with different sets of weights. We select 30 k-bins, $0.001 < k < 0.3\,h\,\mathrm{Mpc}^{-1}$. To test the robustness of the results we repeated the same analysis reducing the maximum k-fitted k_{max} to $0.2\,h\,\mathrm{Mpc}^{-1}$ obtaining fully consistent fits, albeit with increased errors. In method (i) we fit simultaneously monopole and quadrupole (for SGC and NGC with two different windows) adopting a 120 x 120 covariance. In methods (ii) and (iii) we perform a joint fit of the weighted monopole and quadrupole, P_{i,w_j}, each calculated using the appropriate set of weights for q_0 and q_1 (and p_0, p_1).

We compute the covariance matrix from the 1000 EZ mocks used in Ruggeri et al. (2017a), including all weights as

$$C = \frac{1}{999}\sum_{n=1}^{1000}[\mathbf{d}_n(k_i) - \hat{\mathbf{d}}(k_i)][\mathbf{d}_n(k_j) - \hat{\mathbf{d}}(k_j)]^T, \quad (4)$$

where $\mathbf{d}_n$ is the vector formed of the multiple weighted moments being fitted, and $\hat{\mathbf{d}}$ is the mean value. Note that when inverting the covariance matrix we include the small Hartlap factor (Hartlap, Simon & Schneider 2007) and the Dodelson & Schneider error (Dodelson & Schneider 2013) to account for the fact that C is inferred from mock catalogues. An alternative approach would have been to adjust the Gaussian assumption (Sellentin & Heavens 2016).

Parameter constraints are derived from an MCMC routine, optimized for this problem. Multiple chains are run for each fit, and convergence is checked both using the Gelman & Rubin (1992) convergence criteria and by testing consistency of results from independent chains, starting at different positions.

5 RESULTS

In this section, we present the results obtained from the traditional (i), Ω_m (ii), and $f\sigma_8$ (iii) analyses; we first present the results obtained assuming a fixed fiducial distance–redshift relation, i.e. setting $\alpha_{\parallel}$ and $\alpha_{\perp}$ both equal to unity in our pipeline (Section 5.2), while in Section 5.4 we allow them to vary, fitting simultaneously the growth and the geometry. In Section 5.6, we compare the key results of this work with parallel work performed at a single redshift (as in our traditional analysis) in configuration space (Zarrouk et al. 2018) and Fourier space (Gil-Marín et al. 2018), where the analysis has been extended to include the hexadecapole moment of the power spectrum. We also compare our results with the redshift weights based analysis of Zhao et al. (2018) in Section 5.6, which makes a number of different assumptions and explores alternative cosmological models.

Fiducial cosmology: we analyse the data in a flat ΛCDM cosmological model with total and baryonic components $\Omega_m(z = 0) = 0.31$, $\Omega_b(z = 0) = 0.0325$; neutrino masses $\sum m_\nu = 0.06$ eV, amplitude of the clustering $\sigma_8(z = 0) = 0.8$, spectral index $n_s = 0.97$, and dimensionless hubble parameter $h = 0.676$;

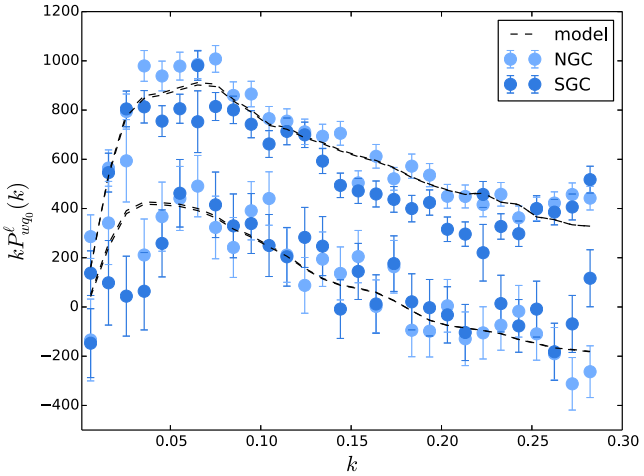

Figure 1. The weighted monopole (top) and quadrupole (bottom) for Ω_m weights; we display the measurement of the weighted moments computed using the NGC (light blue points) and SGC (blue points) samples. The black dashed lines correspond to the best-fitting models obtained from the joint fit of the two samples; the two best-fitting models (dashed lines) differ at large scales because they are convolved with two different window functions accounting for the different survey geometries and systematics between the two samples.

5.1 The weighted multipole measurements

In Fig. 1, we present the moments calculated for the Ω_m set of weights. They all look very similar for all the weights, showing consistency with the fiducial ΛCDM model. It is only if we were to find an inconsistency with this model that we would see an anomaly here for a particular set of weights. i.e. the constraining power lies in the fact that if the cosmology was very different from the fiducial ΛCDM value, these would look very different from each other.

5.2 Fitting growth in a fixed background geometry

As described in Section 3, the traditional analysis constrains the clustering at a single effective epoch allowing for five free parameters: $f\sigma_8(z_p)$, $b\sigma_8(z_p)$ + nuisance parameters. In contrast, the weighted analyses fits the evolution of Ω_m and $f\sigma_8$ with redshift, and requires a fit with seven parameters: q_0, q_1 (p_0, p_1) to model the normalization and evolution in the growth, $b\sigma_8(z_p)\partial b\sigma_8/\partial z$ to account for the evolution in the linear bias $b(z)$, together with nuisance parameters $b_2\sigma_8$, σ_{FoG}, and S. As we are interested in measuring cosmological evolution, we need to carefully consider if the nuisance parameters also need to allow for evolution. Regarding the Fingers-of-God (FoG), it would theoretically be possible to allow this to vary with redshift, but we have checked using N-body simulations that for $k < 0.3\,h\,\mathrm{Mpc}^{-1}$, the evolution does not impact $f\sigma_8$; if we were instead interested in the measurements of non-local bias, for example, allowing for this evolution would have been a key requirement. We do allow the bias to be simultaneously fitted as described in Section 3.

In order to compare the redshift-weight measurements with the traditional one, we projected the seven parameter MCMC chains (q_0, q_1, $b\sigma_8$, $\partial b\sigma_8/\partial z$ + nuisance parameters) into the five-dimension parameter space by computing $f[\Omega_m(q_0, q_1, z_p)]$, $f(p_0, p_1, z_p)$, and $b(z_p)$. The results are displayed in Fig. 2 where we show likelihood contours for $f\sigma_8(z_p)$, $b\sigma_8(z_p)$ etc as derived, obtained from the three different analysis: traditional (brown contours), w_{Ω_m} (blue contours), and $w_{f\sigma_8}$ (green contours) when imposing $\alpha_{\parallel} = \alpha_{\perp} = 1$. It

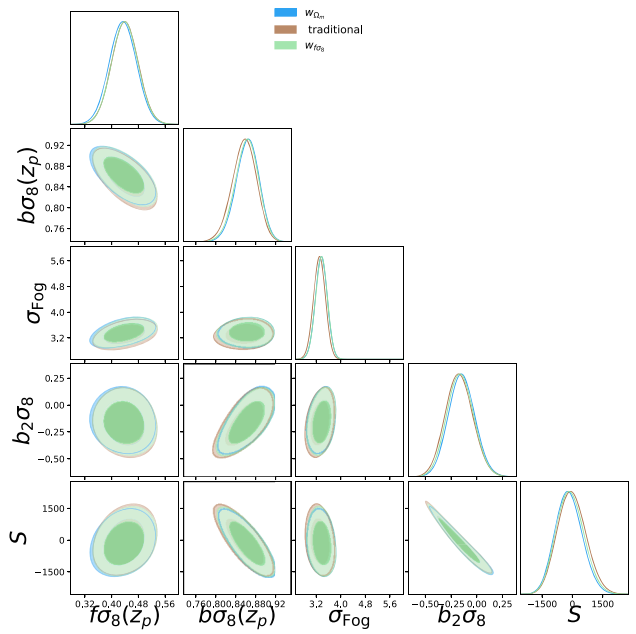

Figure 2. A comparison between the values of $f\sigma_8$, $b\sigma_8$, $\sigma_{\rm FoG}$, S obtained by the three different methods when the background geometry is fixed. The blue and green contours indicate the projected values from the $\Omega_{\rm m}$ and $f\sigma_8$ analyses (seven free parameters), respectively; the brown contours correspond to the constraints obtained from the single-epoch traditional analysis (five free parameters).

is worth noting that all three methods fully agree at the pivot redshift confirming the previous tests made on the mocks (Ruggeri et al. 2017a). Moreover, the redshift weighted analysis give constraints of the same order as those obtained in the traditional analysis even though the latter marginalizes over one less free parameter. This suggests that the information in the data about the evolution of $f\sigma_8$ is available in addition to the information obtained at the effective redshift.

5.3 The evolution of $f\sigma_8(z)$, $\Omega_{\rm m}(z)$, $b(z)$

As described and discussed in Ruggeri et al. (2017a, b), in general, the redshift weights allow us to account for the evolution in the clustering measurements. In this work, through equations (2) and (3) we are able to reconstruct the evolution for $f\sigma_8$ from both q_0, q_1, and p_0, p_1 parameters. We also modelled a linear evolution of the linear bias as described by equation (1). We show the resulting constraints on the evolution of $f\sigma_8$, $b(z)$, $\Omega_{\rm m}(z)$, in Fig. 3.

The lower panel of Fig. 3 shows the evolution in redshift of $f\sigma_8$ obtained applying $w_{\Omega_{\rm m}}$ (blue shaded regions) and $w_{f\sigma_8}$ (green shaded regions). We overplot the constraints coming from the single-epoch (traditional) analysis at redshift 1.52. We find good agreement between the different techniques over the full redshift range. The dashed line indicates the fiducial cosmology used. We detect a similar slope in the evolution to that in the fiducial cosmology, and all of our measurement methods provide results that agree within one sigma with the fiducial cosmology. The error on $f\sigma_8$ increases while moving from the pivot redshift in both directions as uncertainties in q_1 and p_1 become relevant. As we are fixing the projection, varying $\Omega_{\rm m}(z)$ only affects the growth rate, explaining the good agreement between measurements made using both sets of weights; they are both testing for the same sort of departures from the ΛCDM model.

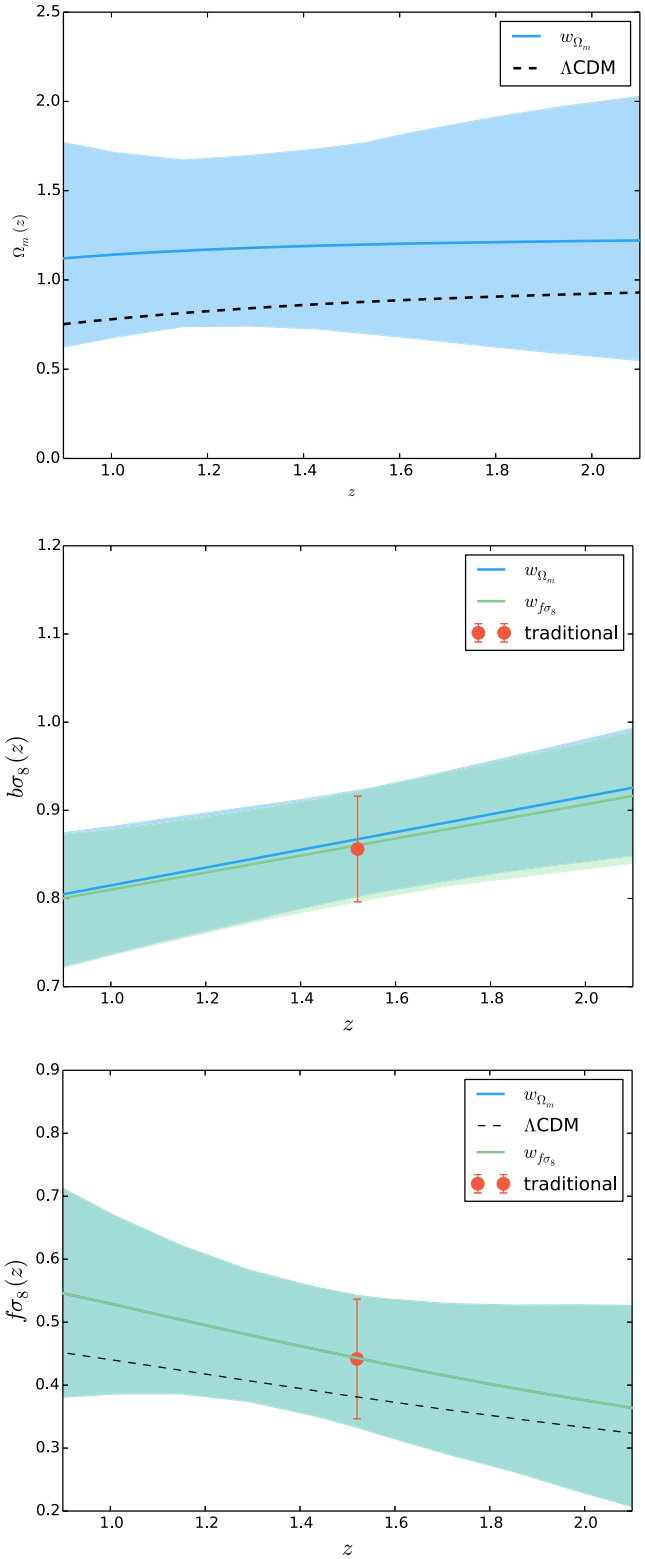

Figure 3. Top Panel: the evolution of $\Omega_{\rm m}(z)$ measured via the parameters q_0, q_1. Middle Panel: the evolution of the linear bias times σ_8 fitted using $\Omega_{\rm m}$ parametrization (blue shaded regions), $f\sigma_8$ parametrizations (green shaded regions); the red point indicates the single-epoch constraints of $b\sigma_8(z_{\rm p})$ from the traditional analysis. Bottom Panel: the evolution of $f\sigma_8$ from the three different analysis (notation and colours as above); all the errors correspond to 68 per cent confidence level.

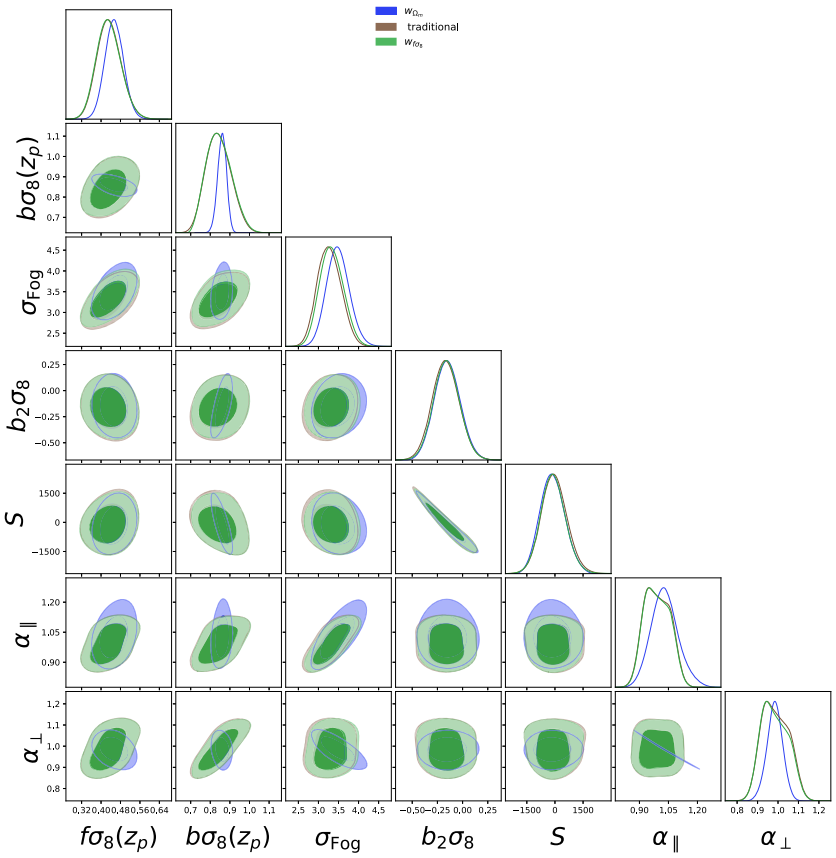

Figure 4. A comparison between the values of $f\sigma_8$, $b\sigma_8$, $\sigma_{\rm FoG}$, S obtained from the three different methods [(i), (ii), (iii)] when the background geometry is allowed to vary through the AP parameters. The green contours correspond to the projected values from the $f\sigma_8$ analysis [$f\sigma_8(p_0, p_1)$, $b\sigma_8(z_p)$, $\sigma_{\rm FoG}$, S, $\alpha_{\rm ||}$, $\alpha_\perp$]. The blue contours represent the projected constraints from Ω analysis [$f\sigma_8(q_0, q_1)$, $b\sigma_8(z_p)$, $\sigma_{\rm FoG}$, S, $\alpha_{\rm ||}(q_0, q_1)$, $\alpha_\perp(q_0, q_1)$]. The brown contours indicate the constraints from the single-epoch traditional analysis at the pivot redshift $z = 1.52$.

The middle panel of Fig. 3 shows our constraints on the linear redshift evolving bias parameter. Also in this case, we find full agreement between the different techniques. As mentioned in Section 3, we do not go beyond linear evolution in the bias, matching our allowed evolution in the cosmological parameters of interest. As we are not interested in the recovered bias parameters, we just want to make sure that the assumptions cannot affect the constraints we get on the growth rate. Ruggeri et al. (2017a) shows that in this case, the linear assumption is valid.

5.4 Simultaneously fitting growth and geometry

We repeat our analysis, using all three methods, but now including the projection (AP) parameters in our models. Given the weak detection of the anisotropic BAO signal in the quasar sample (see Ata et al. 2017), a full fit of the monopole and quadrupole is not enough to give independent strong constraints on the full set of parameters covering both geometrical and growth-rate deviations. i.e. with only wide uniform physical priors on the parameters, the degeneracies between the parameters, particularly the shot noise term together with $f\sigma_8$, $b\sigma_8$ $\alpha_{\rm ||}$, and $\alpha_\perp$, does not allow our chains to converge (after 10^5-10^6 steps). However, as pointed out in Padmanabhan & White (2008), beyond certain values of $\alpha_{\rm ||}$ and $\alpha_\perp$, the full background used to analyse the data loses any meaning. Measurements from independent cosmological probes in almost all cosmological models that we would want to test already put tight constraints on these quantities (Planck Collaboration 2016). We therefore include a broad prior on both $\alpha_{\rm ||}$ and $\alpha_\perp$, setting $0.75 < \alpha_{\rm ||} < 1.25$, $0.85 < \alpha_\perp < 1.25$. To test the robustness of our analysis with respect to the choice of the priors we performed prior-free analysis exploring the likelihood surfaces outside of those regions.

In the traditional and $w_{f\sigma_8}$ analyses we include $\alpha_{\rm ||}$ and $\alpha_\perp$ as two additional free parameters. For the w_{Ω_m} analysis, however, we do not add any further free parameters: we account for the departures from the fiducial geometry by including $\alpha_{\rm ||}[\Omega_{\rm m}(q_0, q_1)]$, $\alpha_\perp[\Omega_{\rm m}(q_0, q_1)]$ in our models (as discussed in Section 3). This procedure requires us to impose a prior on the value of $\Omega_{\rm m}(z)$ which has to be positive definite at any redshift to avoid numerical problem; we illustrate the effect of these prior on the constraints in Fig. 5.

Fig. 4 shows the likelihood contours obtained from the three different analysis when allowing for unknown projection parameters (the AP parameters). The dark brown contours refer to (i); The constraints for the $w_{\Omega_{\rm m}}$, $w_{f\sigma_8}$ analysis (dark blue, $w_{\Omega_{\rm m},{\rm AP}}$ and dark green, $w_{f\sigma_{8,AP}}$) are obtained projecting q_0, q_1 and p_0, p_1 into $f\sigma_8(q_i)$ (p_i); also in this scenario we confirm a good agreement between the three analyses; as explained, $\alpha_{\rm ||}$ and $\alpha_\perp$ are not free in the $w_{\Omega_{\rm m}}$ analysis but we derive them from the constraints of q_0, q_1. This is the reason why the two parameters are highly correlated, as shown in the figure. Note that the $w_{\Omega_{\rm m}}$ method has two less free parameters with respect to $w_{f\sigma_8}$ and one less with respect to the traditional analysis. In Fig. 5, we compare the *evolution* parameters $q_{0,1}$, $b\sigma_8$, $\partial b\sigma_8/\partial z|_{z_{\rm p}}$ obtained (dark blue contours, $w_{\Omega_{\rm m},{\rm AP}}$), with previous results when

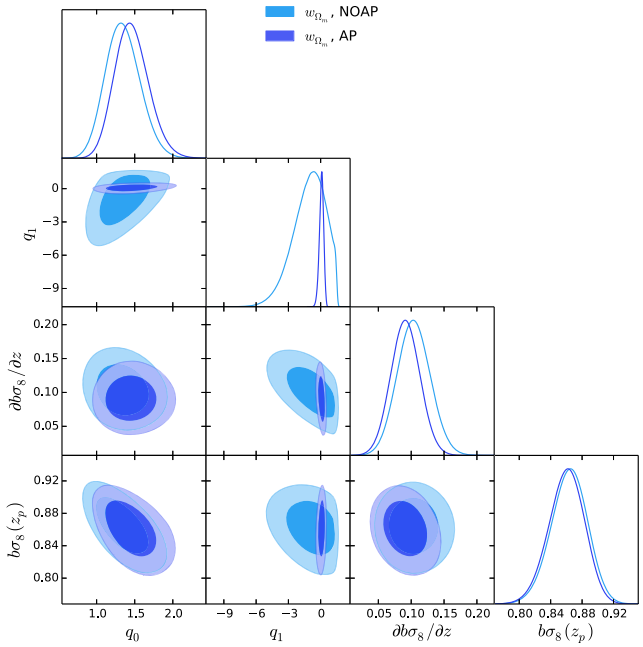

Figure 5. A comparison between the constraints on the *evolution parameters* obtained from the $\Omega_{\rm m}$ analysis with and without fixing the anisotropic projection parameters (blue and light blue contours, respectively).

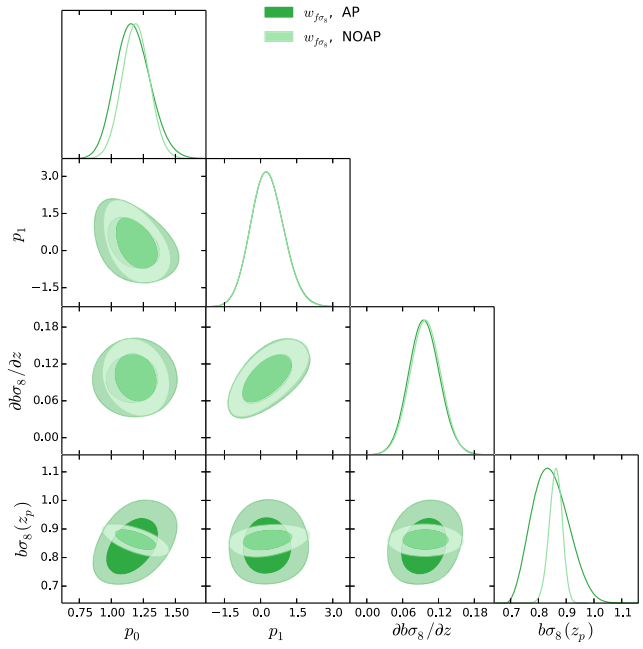

Figure 6. A comparison between the constraints on the *evolution parameters* obtained from the $f\sigma_8$ analysis with and without fixing the anisotropic projection parameters (green and light green contours, respectively).

the geometry has been fixed (blue contours, $w_{\Omega_{\rm m},{\rm NOAP}}$). We find a good agreement between the two; the shapes of q_1 likelihoods show the effect of the physical priors we are including: $\Omega_{\rm m}(z_{\rm p}) > 0$ for $w_{\Omega_m{\rm NOAP}}$ and $\Omega_{\rm m}(z) > 0$, $0.0 < z < 2.2$ for $w_{\Omega_m{\rm AP}}$. Fig. 6 is structured in the same way as Fig. 5; we compare the results from $w_{f\sigma_8,{\rm AP}}$ with previous results of $w_{f\sigma_8,{\rm NOAP}}$ method. We find a good agreement with the best-fitting values obtained; note that here we do not assume physical priors on the sign of $\Omega_{\rm m}$. In Fig. 7, we compare

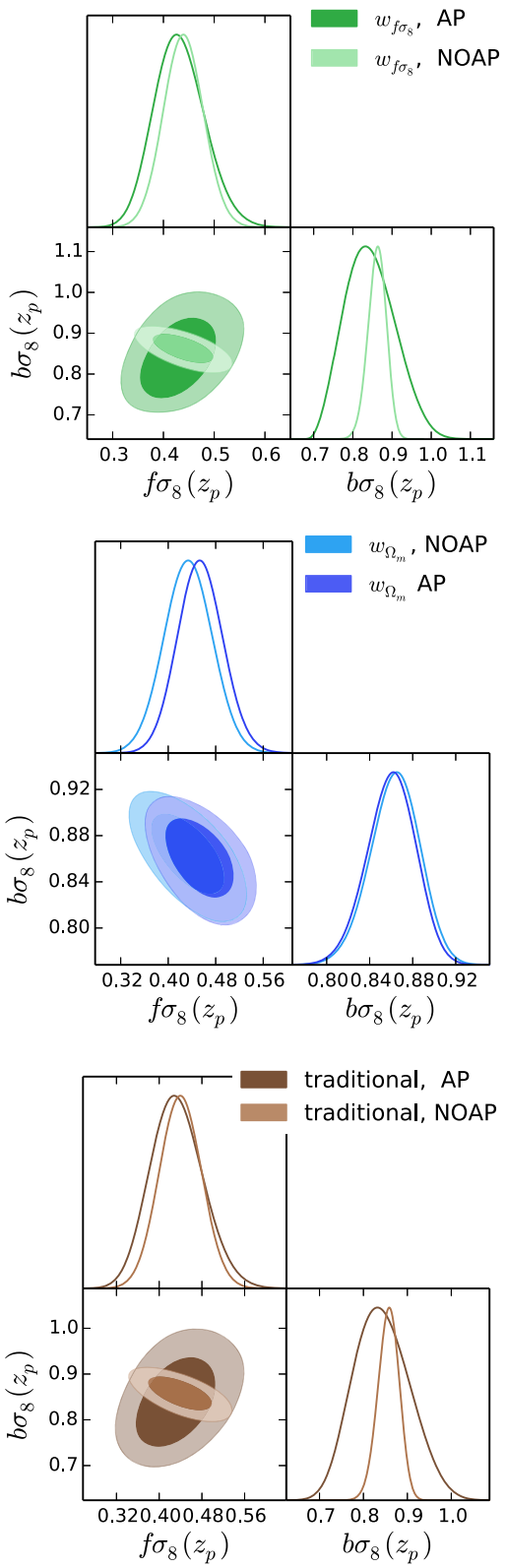

Figure 7. A comparison between the different analysis with AP (darker colours) and without AP (lighter colours). The bottom panel shows the constraints from the traditional analysis of $f\sigma_8(z_{\rm p})$ and $b\sigma_8(z_{\rm p})$. The middle and top panels show the projected constraints of $f\sigma_8(q_0, q_1)$, $b\sigma_8(q_0, q_1)$ (blue and light blue contours) and $f\sigma_8(p_0, p_1)$, $b\sigma_8(p_0, p_1)$ (green and dark green contours) in the $w_{f\sigma_8}$ $w_{\Omega_{\rm m}}$ analysis.

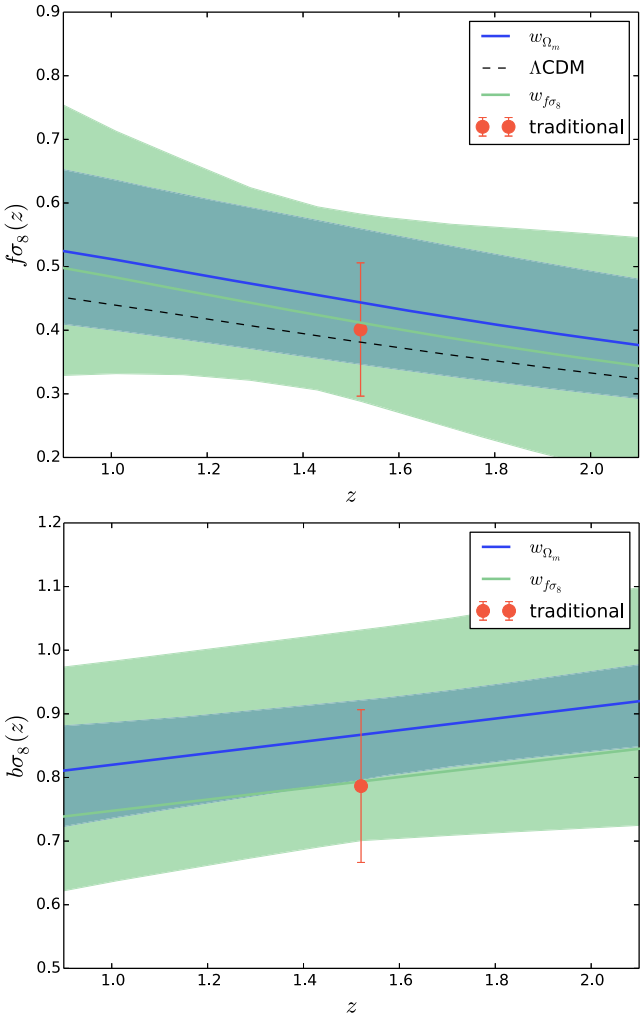

Figure 8. The evolution of $f\sigma_8(z)$ and $b\sigma_8(z)$ when including the AP effect; notation and colours same as in Fig. 3; all the errors correspond to 68 per cent confidence level.

the constraints at the pivot redshift for $f\sigma_8$ and $b\sigma_8$ with and without AP, for method (i), (ii), and (iii) (brown, blue, and green contours); we confirm the good agreement on the constraints for $f\sigma_8$ with and without fixing the geometry. When performing the anisotropic fit we get a larger error as expected; note that for the w_{Ω_m} analysis we get the constraints to be of the same order; as explained, in this scenario, we tie together geometry and growth, thus $\alpha_{\parallel}$ and $\alpha_{\perp}$ are not independent parameters. Finally in Fig. 8, we present the results of the three different analyses, as in Fig. 3. Note that, since in the w_{Ω_m} analysis $\alpha_{\parallel}$ and $\alpha_{\perp}$ are not independent but are included as functions of $\Omega(q_0, q_1, z)$, we obtain a marginalized error smaller than the one obtained in the case of the $w_{f\sigma_8}$ analysis.

5.5 Best-fitting measurements

In Table 1, we summarize the results from the different analysis [(i), (ii), (iii)] with and without free AP parameters (bottom and top panel). We display the best-fitting values (first column) and the mean values $\pm 1\sigma$ (second column). The first section of the table shows the fit to the monopole and quadrupole fixing the AP parameters, while the second section of the table shows the fit results allowing the AP parameters to be simultaneously fitted. The fitting range is $k = 0.01$–$0.3\,h\,\mathrm{Mpc}^{-1}$ for both the monopole and quadrupole. We consider the results from combining both North Galactic Cap (NGC) and South Galactic Cap (SGC) using standard redshifts estimates. The error bars are obtained by marginalizing over all other parameters.

Table 1. The best-fitting measurements for the DR14 quasar data over the redshift range ($0.8 < z < 2.2$). Left-hand panel for results with fixed anisotropic projection parameters (NOAP). Right-hand panel for results with free anisotropic projection parameters (AP). These are the marginalized constraints made from the chains presented in Figs 3, 6, and 8.

Traditional		NOAP	
	max. like.	mean $\pm 1\sigma$	
$f(z)\sigma_8(z)$	0.435	0.44	$\pm$ 0.04
$b\sigma_8$	0.86	0.86	$\pm$ 0.02
σ_{FoG}	3.30	3.30	$\pm$ 0.19
$b_2\sigma_8$	$-$ 0.18	$-$ 0.17	$\pm$ 0.13
S	$-$340	$-$270	$\pm$ 697
χ^2	113/(120 $-$ 5)		
Ω_{m} weights			
q_0	1.31	1.34	$\pm$ 0.23
q_1	$-$ 1.07	$-$ 1.09	$\pm$ 1.50
$b\sigma_8(z_{\mathrm{p}})$	0.10	0.10	$\pm$ 0.025
$\partial b\sigma_8/\partial z\vert_{z_{\mathrm{p}}}$	0.87	0.86	$\pm$ 0.02
σ_{FoG}	3.39	3.34	$\pm$ 0.19
$b_2\sigma_8$	$-$ 0.15	$-$ 0.15	$\pm$ 0.13
S	$-$208	$-$174	$\pm$ 660
χ^2	221/(240 $-$ 7)		
$f\sigma_8$ weights			
p_0	1.11	1.12	$\pm$ 0.11
p_1	0.35	0.28	$\pm$ 0.69
$b\sigma_8(z_{\mathrm{p}})$	0.865	0.86	$\pm$ 0.02
$\partial b\sigma_8/\partial z\vert_{z_{\mathrm{p}}}$	0.10	0.10	$\pm$ 0.03
σ_{FoG}	3.33	3.37	$\pm$ 0.19
$b_2\sigma_8$	$-$ 0.15	$-$ 0.16	$\pm$ 0.13
S	$-$218	$-$106	$\pm$ 676
χ^2	223/(240 $-$ 7)		
$f(z)\sigma_8(z)$	0.40	0.43	$\pm$ 0.05
$b\sigma_8$	0.79	0.84	$\pm$ 0.06
σ_{FoG}	3.0	3.2	$\pm$ 0.29
$b_2\sigma_8$	$-$ 0.16	$-$ 0.17	$\pm$ 0.13
S	28	$-$37	$\pm$ 685
$\alpha_{\parallel}$	0.95	0.99	$\pm$ 0.065
$\alpha_{\perp}$	0.94	0.99	$\pm$ 0.06
χ^2	112/(120 $-$ 7)		
Ω_{m} weights			
q_0	1.42	1.46	$\pm$ 0.22
q_1	0.07	0.07	$\pm$ 0.20
$b\sigma_8(z_{\mathrm{p}})$	0.86	0.09	$\pm$ 0.02
$\partial b\sigma_8/\partial z\vert_{z_{\mathrm{p}}}$	0.09	0.09	$\pm$ 0.02
σ_{FoG}	3.44	3.48	$\pm$ 0.28
$b_2\sigma_8$	$-$ 0.16	$-$ 0.15	$\pm$ 0.13
S	$-$145	$-$124	$\pm$ 653
χ^2	222/(240 $-$ 7)		
$f\sigma_8$ weights			
p_0	1.11	1.11	$\pm$ 0.13
p_1	0.16	0.29	$\pm$ 0.69
$b\sigma_8(z_{\mathrm{p}})$	0.79	0.85	$\pm$ 0.06
$\partial b\sigma_8/\partial z\vert_{z_{\mathrm{p}}}$	0.09	0.10	$\pm$ 0.03
σ_{FoG}	3.19	3.33	$\pm$ 0.29
$b_2\sigma_8$	$-$ 0.13	$-$ 0.16	$\pm$ 0.13
S	$-$205	$-$95	$\pm$ 664
$\alpha_{\parallel}$	0.94	0.99	$\pm$ 0.06
$\alpha_{\perp}$	0.94	0.98	$\pm$ 0.06
χ^2	222/(240 $-$ 9)		

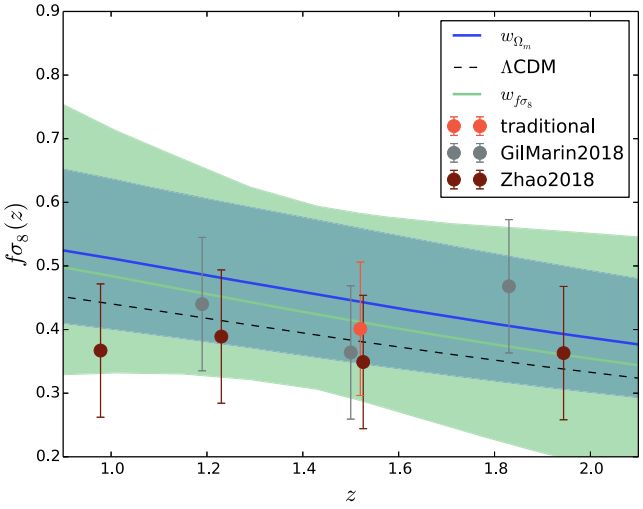

Figure 9. Comparison of $f\sigma_8$ evolution as obtained by different analysis. All the errors correspond to 68 per cent confidence level.

5.6 Consensus with other projects

The current analysis has been compared with similar analysis performed on the same data set (Gil-Marín et al. 2018; Hou et al. 2018; Zarrouk et al. 2018; Zhao et al. 2018). We refer to Zarrouk et al. (2018) for a longer discussion on the different methodologies and we here focus only on the comparison between analyses measuring the redshift evolution of the growth rate. In particular, we compare our results with analyses presented in Gil-Marín et al. (2018) and Zhao et al. (2018). In Gil-Marín et al. (2018), the evolution of $f\sigma_8$ has been studied performing an analysis in three different overlapping redshift bins: $0.8 < z < 1.5$, $1.2 < z < 1.8$, $1.5 < z < 2.2$, corresponding to effective redshifts: 1.19, 1.5, 1.83. This standard analysis considers the first three moments of the power spectrum, $P_{0,2,4}$, up to $k = 0.3\,h\,\mathrm{Mpc}^{-1}$; the measurements are fitted with the TNS model computed up to two-loop in SPT; the window survey effect is accounted following Wilson et al. (2017). In Zhao et al. (2018) they perform a joint BAO and RSD analysis using the monopole and quadrupole (in the k-range of $0.02 \leq k\,[h\mathrm{Mpc}^{-1}] \leq 0.30$) and comparing with a TNS redshift-space power spectrum template at two-loop level in perturbation theory. They derive redshift weights following the lines of Zhu et al. (2015) and Ruggeri et al. (2017b) to optimize the constraints on $\alpha_\perp$, $\alpha_\parallel$, and $f\sigma_8$ at four effective redshifts, namely, $z_{\rm eff} = 0.98$, 1.23, 1.53, and 1.94. In contrast to the analysis presented in this work where the whole redshift range is considered and the weighted multipoles are combined in a joint fit; in Zhao et al. (2018), the redshift weights act to divide the sample into *smooth* z-bins. In each bin they perform the same analysis to constrain $f\sigma_8(z_{\rm eff})$, $\alpha_{\parallel,\perp}(z_{\rm eff})$ at the four effective redshifts. Thus, this approach is a hybrid between redshift weighting and standard analyses. Zhao et al. (2018) use an optimization to find the best redshift kernels and then perform a standard analysis for each, assuming the measurements being at one effective redshift. In contrast, we directly measure parameters controlling the redshift evolution. In Fig. 9, we show the constraints from the different analysis. The red point and blue and green bands correspond to the traditional and redshift weight analysis results [(i), (ii), (iii)] presented in this work. The grey points correspond to the redshift bin analysis presented in Gil-Marín et al. (2018), while dark red points correspond to the analysis of Zhao et al. (2018). We confirm the good agreement between the different techniques in measuring $f\sigma_8(z)$. Note that the marginalized error bars for the red, grey, dark red points refer to analyses with seven free parameters [$f\sigma_8(z_{\rm eff})$, $b\sigma_8(z_{\rm eff})$, $\alpha_\parallel$, $\alpha_\perp$ + nuisance], while redshift weights methods (blue and green band) include seven and nine free parameters (q_0, q_1, $b\sigma_8$, $\partial b\sigma_8/\partial z$ + *nuisance*) and (p_0, p_1, $b\sigma_8$, $\partial b\sigma_8/\partial z\alpha_{\parallel}$, $\alpha_\perp$ + *nuisance*), respectively.

6 DISCUSSION

The DR14 quasar sample allows for tests of the cosmological model at previously unexplored epochs; further, as it also cover a wide redshift range (0.8−2.2), it opens up the possibility of directly investigating the evolution of the cosmological parameters. Standard analyses (e.g. Alam et al. 2016) investigate the evolution of the growth rate at different epochs by cutting their volume into redshifts slices. The quasar sample is characterized by a low density compared to previous samples, such as the BOSS LRG sample, thus the bin-cutting can have a significant impact on the resulting S/N.

In this work, we choose to constrain the growth rate and its first derivative in redshift considering the full redshift range, using optimal redshift weighting techniques; redshift weights act as a smooth window on the data, compressing the correlation in the redshift direction, while keeping track of the underlying evolution of the clustering. We select the optimal redshift weights as they are predicted through the Fisher matrix. The weights specific for the growth measurements have been derived in Ruggeri et al. (2017b) and tested in Ruggeri et al. (2017a).

We explore two different parametrizations to model the evolution in redshift of $f\sigma_8$; the first models the evolution in redshift through $\Omega_{\rm m}(z)$. This parametrization allows us to account simultaneously for deviations in both geometry and growth with respect to the ΛCDM scenario. The second, investigates deviations in the evolution of $f\sigma_8(z)$ about the fiducial cosmology; in this case the growth and the geometry deviations are artificially kept separated.

To compare the constraints on $f\sigma_8$ with the *traditional* method, performed at a single epoch, we computed $f\sigma_8(z_{\rm p})$ from the evolving constraints, finding full agreement between the three different methods.

We perform the same analysis first by fixing the geometrical projection, given by H, D_A; in this case as expected both redshift weight methods give exactly the same constraints of $f\sigma_8$. We then considered an anisotropic fit, including the AP parameters in our models. In this case the constraints from $\Omega_{\rm m}(z)$ differ with the other analysis since $\alpha_{\parallel,\perp}$ are not included as free independent parameters but their evolution is described through $\Omega_{\rm m}(z)$. Also in this scenario we find good agreement (within 1σ) between the parameters of interest.

In this and in Ruggeri et al. (2017a, b) we showed step by step how to include the redshift weights in the analysis; we also showed how easily to account for the evolution in the models by re-deriving the window function and confirmed that the redshift weights method gives unbiased constraints. Future surveys are expected to reduce the statistical error by an order of magnitude over a wide redshift range. Therefore, it will be increasingly important to account for the evolution in the models. The extent of the dynamical redshift range covered, by for example DESI (Levi et al. 2013), will open up the possibility to discriminate between different cosmological scenarios. This will be accomplished using the evolution of the key-parameters to remove part of the degeneracy between them.

ACKNOWLEDGEMENTS

RR and WJP acknowledge support from the European Research Council through the Darksurvey grant 614030. RR also thanks Dr. Violeta Gonzalez-Perez, Dr. Hans Winther, Dr. Seshadri Nadathur, Iza Pstrucha, and Gary Burton. WJP also acknowledges support from the UK Science and Technology Facilities Council grant ST/N000668/1, and the UK Space Agency grant ST/N00180X/1. Funding for SDSS-III and SDSS-IV has been provided by the Alfred P. Sloan Foundation and Participating Institutions. Additional funding for SDSS-III comes from the National Science Foundation and the U.S. Department of Energy Office of Science. Further information about both projects is available at http://www.sdss.org. SDSS is managed by the Astrophysical Research Consortium for the Participating Institutions in both collaborations. In SDSS-III, these include the University of Arizona, the Brazilian Participation Group, Brookhaven National Laboratory, Carnegie Mellon University, University of Florida, the French Participation Group, the German Participation Group, Harvard University, the Instituto de Astrofisica de Canarias, the Michigan State / Notre Dame / JINA Participation Group, Johns Hopkins University, Lawrence Berkeley National Laboratory, Max Planck Institute for Astrophysics, Max Planck Institute for Extraterrestrial Physics, New Mexico State University, New York University, Ohio State University, Pennsylvania State University, University of Portsmouth, Princeton University, the Spanish Participation Group, University of Tokyo, University of Utah, Vanderbilt University, University of Virginia, University of Washington, and Yale University. The Participating Institutions in SDSS-IV are Carnegie Mellon University, Colorado University, Boulder, Harvard- Smithsonian Center for Astrophysics Participation Group, Johns Hopkins University, Kavli Institute for the Physics and Mathematics of the Universe Max-Planck-Institut fuer Astrophysik (MPA Garching), Max-Planck-Institut fuer Extraterrestrische Physik (MPE), Max-Planck-Institut fuer Astronomie (MPIA Heidelberg), National Astronomical Observatories of China, New Mexico State University, New York University, The Ohio State University, Penn State University, Shanghai Astronomical Observatory, United Kingdom Participation Group, University of Portsmouth, Univer- sity of Utah, University of Wisconsin, and Yale University. This work used the facilities and staff of the UK Sciama High Performance Computing cluster supported by the ICG, SEPNet, and the University of Portsmouth. This research used resources of the National Energy Research Scientific Computing Center, a DOE Office of Science User Facility supported by the Office of Science of the U.S. Department of Energy, under Contract No. DE-AC02-05CH11231.

REFERENCES

Aihara H. et al., 2011, ApJS, 193, 29
Alam S. et al., 2017, MNRAS, 470, 2617
Alcock C., Paczynski B., 1979, Nature, 281, 358
Ata M. et al., 2017, MNRAS, 467, 3993
Baldauf T., Seljak U., Desjacques V., McDonald P., 2012, Phys. Rev., 86, 083540
Bianchi D., Gil-Marín H., Ruggeri R., Percival W. J., 2015, MNRAS, 453, L11
Blanton M. R. et al., 2017, AJ, 154, 28
Bolton A. S. et al., 2012, AJ, 144, 144
Chan K. C., Scoccimarro R., Sheth R. K., 2012, Phys. Rev., 85, 083509
Croom S. M., Smith R. J., Boyle B. J., Shanks T., Miller L., Outram P. J., Loaring N. S., 2004, MNRAS, 349, 1397
Dawson K. S. et al., 2016, AJ, 151, 44
Dodelson S., Schneider M. D., 2013, Phys. Rev., 88, 063537
Feldman H. A., Kaiser N., Peacock J. A., 1994, ApJ, 426, 23
Gelman A., Rubin D., 1992, Stat. Sci., 7, 457
Gil-Marín H. et al., 2018, MNRAS, 477, 1604
Gunn J. E. et al., 2006, AJ, 131, 2332
Gunn S. R., 1998, Support Vector Machines for Classification and Regression
Habib S. et al., 2016, New Astron., 42, 49
Hartlap J., Simon P., Schneider P., 2007, A&A, 464, 399
Hou J. et al., 2018, MNRAS, 480, 2521
Laurent P. et al., 2017, J. Cosmol. Astropart. Phys., 7, 17
Levi M. et al., 2013, preprint (arXive: 1308.0847)
Lewis A., Bridle S., 2002, Phys. Rev., 66, 103511
Mueller E.-M., Percival W. J., Ruggeri R., 2018, MNRAS, preprint (arXiv: 1702.05088)
Myers A. D. et al., 2015, ApJS, 221, 27
Padmanabhan N., White M., 2008, Phys. Rev., 77, 123540
Pâris I. et al., 2018, A&A, 613, A51
Planck Collaboration, 2016, A&A, 594, A13
Ruggeri R., Percival W. J., Mueller E.-M., Gil-Marin H., Zhu F., Padmanabhan N., Zhao G.-B., 2017a, preprint (arXiv:1712.03997)
Ruggeri R., Percival W. J., Gil-Marín H., Zhu F., Zhao G.-B., Wang Y., 2017b, MNRAS, 464, 2698
Saito S., Baldauf T., Vlah Z., Seljak U., Okumura T., McDonald P., 2014, Phys. Rev., 90, 123522
Sellentin E., Heavens A. F., 2016, MNRAS, 456, L132
Smee S. A. et al., 2013, AJ, 146, 32
Taruya A., Nishimichi T., Saito S., 2010, Phys. Rev., 82, 063522
Wang D. et al., 2018, MNRAS, 477, 1528
Wilson M. J., Peacock J. A., Taylor A. N., de la Torre S., 2017, MNRAS, 464, 3121
Wright E. L. et al., 2010, AJ, 140, 1868
Zarrouk P. et al., 2018, MNRAS, 477, 1639
Zhao G.-B. et al., 2016, MNRAS, 457, 2377
Zhao G.-B. et al., 2019, MNRAS, 482, 3497
Zhu F. et al., 2018, MNRAS, 480, 1096
Zhu F., Padmanabhan N., White M., 2015, MNRAS, 451, 236
Zhu F., Padmanabhan N., White M., Ross A. J., Zhao G., 2016, MNRAS, 461, 2867

This paper has been typeset from a TEX/LATEX file prepared by the author.